# Experiments and analysis of drainage displacement processes relevant to carbon dioxide injection

Saman A. Aryana and Anthony R. Kovscek
*Department of Energy Resources Engineering, Stanford University, Stanford, California 94305, USA*
(Received 26 March 2012; published 13 December 2012)

The motivation for this work is a dramatically improved understanding of the fluid mechanics of drainage processes with applications such as $CO_2$ storage in saline aquifers and water-alternating-gas injection as an enhanced oil recovery method. In this paper we present *in situ* distributions of wetting and nonwetting fluids obtained during core-scale two-phase immiscible drainage experiments. The ratio of the viscosity of the resident fluid to that of the invading fluid varies across a range of 0.43 to 150. Saturation distributions observed during dynamic displacement experiments are surprisingly smooth and do not display only one or a few dominant fingers, contrary to the indications of the current literature. The analysis of the saturation distribution using the fractal dimensions of the dynamic three-dimensional saturation distributions suggests that the constitutive relationships for porous media, namely, the relative permeability functions, are history dependent. Accordingly, it is suggested that the nonlinear, unstable flow regime is the regime where efforts to improve physical understanding must be focused.

DOI: 10.1103/PhysRevE.86.066310 PACS number(s): 47.56.+r

## I. INTRODUCTION

Multiphase flow associated with $CO_2$ sequestration in geological saline formations and injection of slugs of $CO_2$ as part of enhanced oil recovery schemes is complex. A fundamental understanding of two-phase, immiscible flow in natural porous media across a range of parameters, i.e., viscosity ratios, helps us understand the behavior and develop models that approximate physics more closely. Capillary, viscous, and gravitational forces determine the dynamics of two-phase, immiscible flow. The relative magnitude of these forces are often quantified as

$$N_{ca} = \frac{U\mu}{\sigma} \quad \text{(capillary number)}, \tag{1}$$

$$M = \frac{\lambda_i}{\lambda_r} \quad \text{(mobility ratio)}, \tag{2}$$

$$\text{Bo} = \frac{\Delta\rho g d^2}{\sigma} \quad \text{(Bond number)}, \tag{3}$$

where the subscripts $i$ and $r$ refer to the invading and resident phases, respectively, $U$ is the invading phase Darcy velocity, $\mu$ is viscosity, $\sigma$ is the interfacial tension, $\lambda$ is phase mobility, $\Delta\rho$ is the difference in density between the two phases (resident and invading), $g$ is acceleration due to gravity, and $d$ is a characteristic distance. The current challenges in formulating multiphase dynamics arise from the difficulty in characterizing the heterogeneity and complexity inherent in natural geological porous media and the instability of the flow dynamics due to large differences in density and viscosity between $CO_2$ and the resident fluid. Significant research has been conducted to date to characterize unstable multiphase flow processes [1–7]. Nevertheless, multiscale experimental data suggest current models are lacking in terms of predictive capabilities [1,8,9].

The objective of this research is to investigate the relevant physical mechanisms responsible for instabilities during drainage (i.e., nonwetting phase injection) via detailed experimentation. In this effort, we investigate the flow dynamics of drainage processes via core-scale experiments across a range of viscosity ratios. The following section describes the apparatus, methods, and fluid pairs. An analysis of the data follows along with the results. The analysis comprises two parts. The first part presents a comparison between the wavelength of perturbations on the interface between the two fluids in the displacement experiments and the predictions of linear stability analysis. The second part explores the self-similar and fractal characteristics of the experimental saturation distribution. The analysis reveals the time dependence of the two-phase fractional flow function and as a consequence the constitutive relationships for porous media.

## II. EXPERIMENTS

The experimental apparatus used in this research includes a Teledyne ISCO 500D syringe pump, a Berea Sandstone core placed in an aluminum sleeve and potted with epoxy, and eight differential pressure Celesco transducers (one at the inlet, one at the outlet, and six along the core at 10-cm intervals). The setup is shown in Fig. 1. Core characterization and *in situ* measurements of saturation distributions are obtained using an x-ray computerized tomography (CT) scanner (GE HiSpeed CT/i helical CT). The spatial resolution of the measurements is determined by voxel volume, which is 0.195 $mm^2 \times 3$ mm along the length of core. Due to practical limitations on the number and frequency of scans, 12 sections along the length of core are scanned throughout the experiments. Raw CT data are processed to obtain porosity and phase saturation distributions. According to Beer's law, the porosity for each voxel is determined as

$$\phi = \frac{\chi_{\text{wet}} - \chi_{\text{dry}}}{\chi_w - \chi_a}, \tag{4}$$

where $\chi$ is proportional to x-ray attenuation as a result of its passage through the setup and is measured in units of Hounsfield (H). $\chi_{\text{wet}}$ and $\chi_{\text{dry}}$ refer to CT numbers associated with fully water and air saturated rock, respectively. $\chi_w$ and $\chi_a$ represent CT numbers associated with pure water and air, respectively. The nonwetting phase saturation for each voxel

 

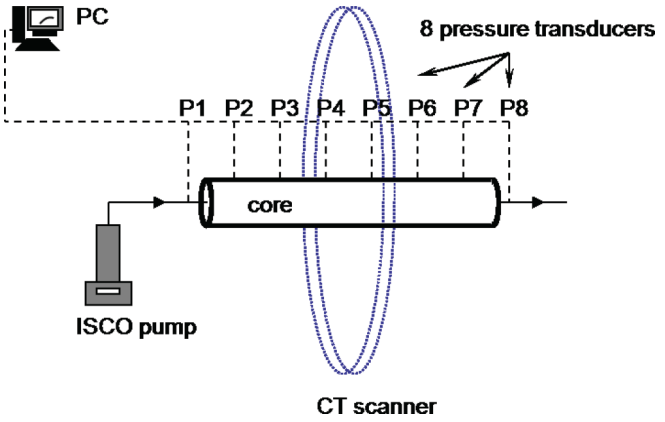


FIG. 1. (Color online) Experimental setup.

is calculated as

$$S_n = \frac{\chi_{\text{exp}} - \chi_{\text{wet}}}{\phi\,(\chi_n - \chi_w)}, \tag{5}$$

where $\chi_{\text{exp}}$ are CT numbers associated with the rock during experiments, $\chi_{\text{wet}}$ are CT numbers obtained while the rock is fully saturated with a wetting phase, $\phi$ is the voxel-by-voxel matrix of porosity at the particular image location, and $\chi_w$ and $\chi_n$ are CT numbers of pure wetting and nonwetting phases, respectively. Equations (4) and (5) yield porosity and saturation values for voxels that make up the scanned sections of the core. The values corresponding to points in the rock between the scanned sections are calculated using a linear interpolation between the sections.

The core is a Berea Sandstone cylinder of 5.08 cm in diameter and 60 cm in length (Cleveland Quarries). The core is strongly water-wet and has an average porosity of 0.19 and permeability of 0.25 D ($\mu$m$^2$). The average porosity at each scan location is shown in Fig. 2. The rock is characterized as fairly homogeneous, especially in the cross sections normal to flow where little variation in porosity is measured.

The experiments are conducted using pairs of fluids that are analogous to $CO_2$ injection into saline aquifers in the sense that the viscosity ratio is characteristic of the two fluids in each pair during drainage processes. The fluid pairs are

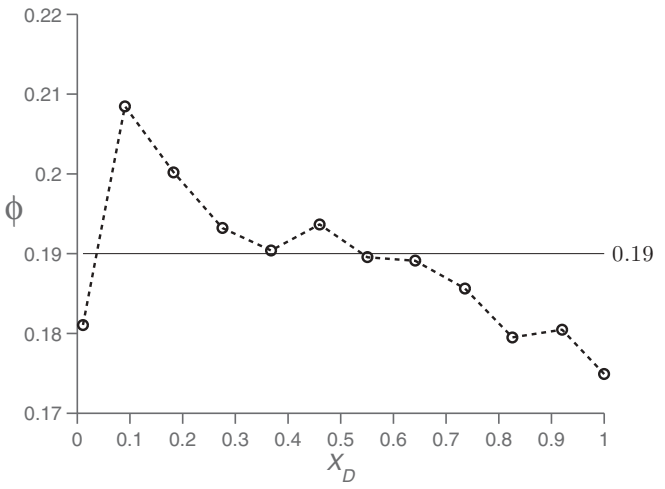


FIG. 2. Porosity profile along sandstone core.

TABLE I. Experimental fluids and capillary numbers.

| Experiment | Invading | Resident | $v_r$ [a] | $N_{ca}$ |
|---|---|---|---|---|
| 1 | n-decane | brine[b] | 1.1 | $2 \times 10^{-7}$ |
| 2 | isooctane[c] | brine[b] | 2.1 | $3 \times 10^{-7}$ |
| 3 | n-heptane | brine[b] | 2.6 | $3 \times 10^{-7}$ |
| 4 | n-hexane | brine[b] | 3.2 | $4 \times 10^{-7}$ |
| 5 | n-pentane | brine[b] | 4.4 | $4 \times 10^{-7}$ |
| 6 | n-decane | mix15[d] | 15.0 | $1 \times 10^{-6}$ |
| 7 | n-decane | mix10[e] | 10.0 | $2 \times 10^{-6}$ |
| 8 | n-decane | mix20[f] | 19.7 | $3 \times 10^{-6}$ |
| 9 | n-decane | mix30[g] | 30.0 | $4 \times 10^{-6}$ |
| 10 | n-pentane | mix150[h] | 150.0 | $8 \times 10^{-6}$ |
| 11 | white mineral oil | mix15[d] | 0.43 | $5 \times 10^{-5}$ |

[a]Viscosity ratio.
[b]8% (by weight) sodium bromide solution,
[c]2,2,4-Trimethylpentane.
[d]Mixture of 8% (by weight) sodium bromide solution and glycerin at a volume ratio of 5:8.
[e]Mixture of 8% (by weight) sodium bromide solution and glycerin at a volume ratio of 11:12.
[f]Mixture of 8% (by weight) sodium bromide solution and glycerin at a volume ratio of 11:21.
[g]Mixture of 8% (by weight) sodium bromide solution and glycerin at a volume ratio of 25:61.
[h]Mixture of 8% (by weight) sodium bromide solution and glycerin at a volume ratio of 46:125.

also analogous to the gas-water displacement of a water-alternating-gas injection process. Major factors contributing to the choice of pairs of analogous fluids include the following: (1) target injection rates and viscosity ratios of interest are achieved while the experimental setup is under much lower average pressure than would be required if $CO_2$ was used in experiments, and (2) a much wider range of viscosity ratios are examined than would be possible with $CO_2$ and saline solutions. The pairs of fluids are listed in Table I. The two fluids of each pair are placed in contact with each other for several hours prior to preparation of the experimental setup to minimize dissolution during displacement experiments. The pre-equilibration process minimizes mass transfer across the interface between fluids during experiments. Subsequently, the immiscibility assumption is more accurate and the observed dynamics of flow is attributable to the fluid mechanics and the relevant physical mechanisms. Sodium bromide (NaBr) (8% by weight) is dissolved in the wetting phase in all experiments to increase the contrast between the CT numbers of the wetting and nonwetting phases and to minimize the possibility of heaving of any clay particles that may reside in the natural porous medium.

Prior to each experiment, the core is fully saturated with the wetting phase. During displacement experiments, the nonwetting phase is injected at a rate of 1.41 cm$^3$/min, which translates to $U = 1$ m/day and the core is scanned at prescribed time intervals. The analogous sets of fluids used in experiments are listed in Table I. Foster [10] and Gupta and Trushenski [11] established the critical capillary number and the total desaturation capillary number for Berea Sandstone using brine and oil (decane in Gupta and Trushenski's case) to be in

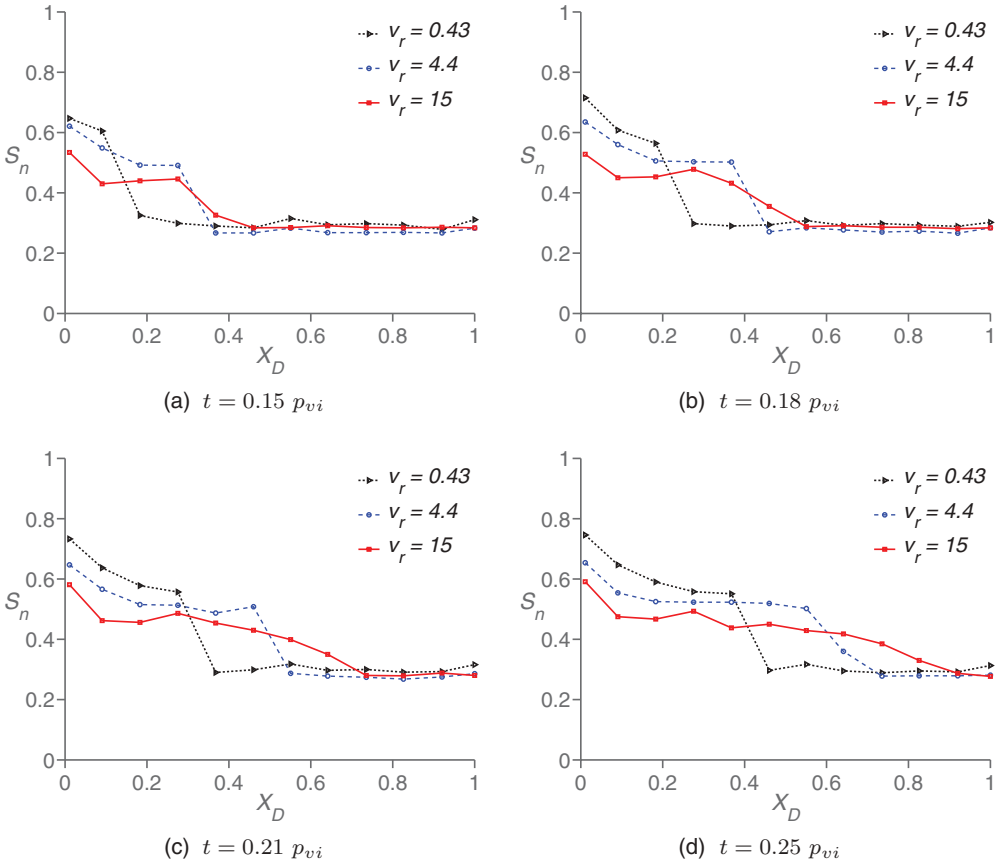


FIG. 3. (Color online) One-dimensional saturation profiles for experiments 11 ($v_r = 0.43$, dotted black line with right triangles), 5 ($v_r = 4.4$, bold dashed blue line with circles), and 6 ($v_r = 15$, solid red line with squares) (a) at time = 0.15 pore volume injected, (b) at time = 0.18 pore volume injected, (c) at time = 0.21 pore volume injected, and (d) at time = 0.25 pore volume injected.

the range of $10^{-5}$–$10^{-4}$ and $10^{-2}$–$10^{-1}$, respectively. Hence, the flow dynamics in our experiments is viscous dominated. The experiments described herein are drainage processes with viscosity ratios ($v_r$; defined as the ratio of viscosity of the resident fluid to that of the invading fluid at 20 °C) ranging from 0.43 to 150.

## III. RESULTS AND ANALYSIS

Experiments cover a range of viscosity ratios spanning from more stable ($v_r = 0.43$) to quite unstable displacements ($v_r = 150$). The evolution of the one-dimensional saturation distributions for experiments 11, 5, and 6 (viscosity ratio = 0.43, 4.4, 15, respectively) are representative and presented in Fig. 3. The three profiles corresponding to the different viscosity ratios in each subfigure are at the same time. From subfigure (a) to (d), the time spans from 0.15 to 0.25 pore volume injected ($p_{vi}$). All times precede breakthrough of the nonwetting phase to the core outlet. There is an effect on the displacement as the tests transition to less stable conditions. Clearly, the degree of desaturation diminishes and the fronts become more dispersed. For experiment 6 with $v_r$ equal to 15, the displacement front is hardly recognizable, especially for times greater than 0.21 $p_{vi}$. The displacement appears to be mostly dispersed and resembles a rarefaction rather than a shock.

Three-dimensional surfaces highlighting the spatial distribution of the nonwetting-phase saturation of the middle of the displacement front are shown in Figs. 4–6 for viscosity ratios of 0.43, 4.4, and 15, respectively. The choice of the nonwetting-phase saturation in each experiment to construct the surfaces impacts the position of the surfaces along the core. The rugosity of these surfaces, however, is insensitive to the $S_{nw}$ chosen. The time sequences in Figs. 4 to 6 are evenly spaced and identical in each figure, and sufficient spatial detail is given for one to view the lack of emergence of dominant fingers. While the average saturation front is clearly more dispersed at greater viscosity ratios as shown in Fig. 3, Figs. 4 to 6 demonstrate that the nature of this dispersed front is the emergence of a great number of fingers that are small in the flow direction as well as normal to it. There seems to be a significant amount of local instability around the front that does not translate into a few dominant fingers engulfing all the other fingers and propagating in the direction of flow.

### A. Linear stability analysis

It has been demonstrated through experiments [2,7,12–16] that in a displacement process where the invading fluid is less viscous than the resident fluid the interface exhibits instabilities that appear in the form of spatial perturbations of the moving displacement front from the plane interface

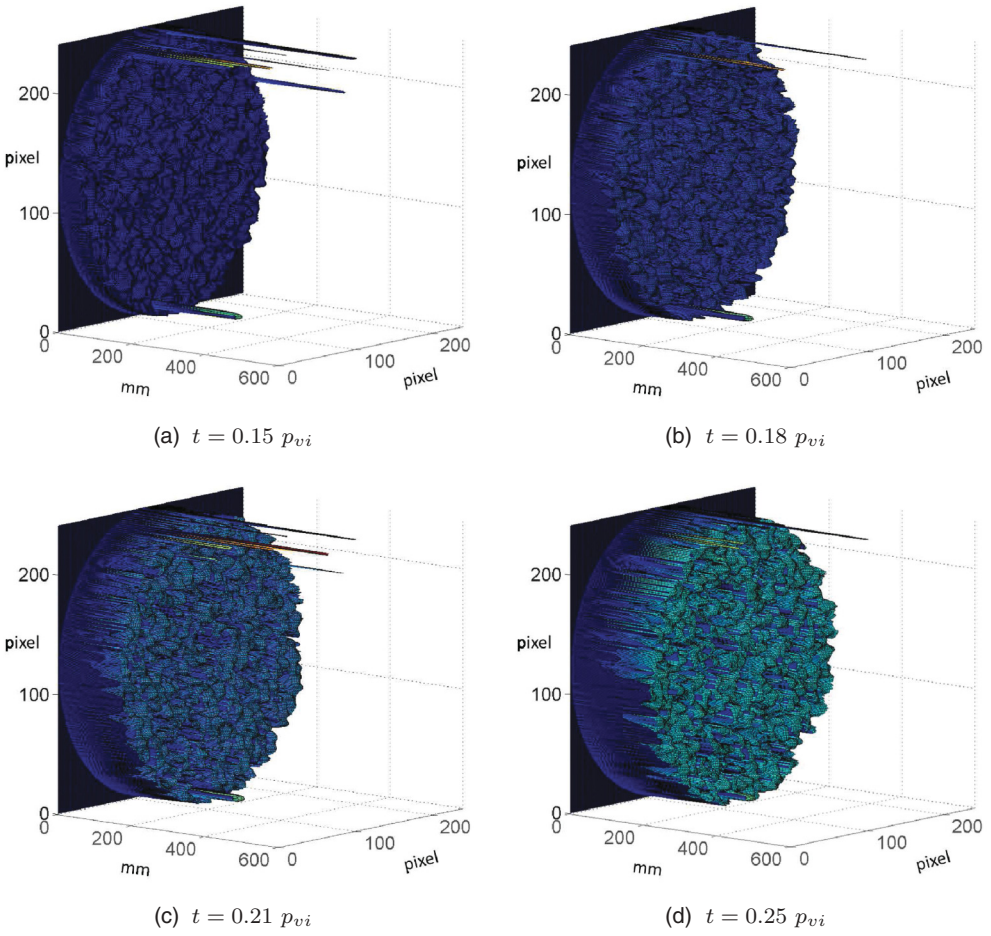


(a) $t = 0.15\ p_{vi}$ (b) $t = 0.18\ p_{vi}$

(c) $t = 0.21\ p_{vi}$ (d) $t = 0.25\ p_{vi}$

FIG. 4. (Color online) Spatial distribution of shock nonwetting-phase saturation ($S_{nw} = 0.55$) for experiment 11 ($v_r = 0.43$) (a) at time = 0.15 pore volume injected, (b) at time = 0.18 pore volume injected, (c) at time = 0.21 pore volume injected, and (d) at time = 0.25 pore volume injected. In each subfigure, the axis corresponding to the length of the core is represented in millimeters. The other two axes are represented in pixels where 1 pixel $\approx$ 0.195 mm.

between the two fluids. As a preliminary step to further analysis, we apply the linear stability analysis of an interface under the influence of viscous, gravity, and capillary forces as outlined by Chuoke *et al.* [17]. The modes of these deformations are greater than a critical wavelength, $\lambda_c$, given by

$$\lambda_c = 2\pi\sqrt{\frac{\sigma^* K}{U(\mu_r - \mu_i)}}. \tag{6}$$

The wavelength (twice the finger width) of maximum instability, $\lambda_m$, is calculated by

$$\lambda_m = 2\sqrt{3}\pi\sqrt{\frac{\sigma^* K}{U(\mu_r - \mu_i)}}. \tag{7}$$

In these equations $\mu_r$ and $\mu_i$ refer to viscosity of the resident and invading fluids, respectively, $K$ is the absolute permeability of the medium, $U$ is the injection Darcy velocity, and $\sigma^*$ is an effective interfacial tension. A basic assumption is that instabilities occur when $(\mu_r - \mu_i) > 0$.

Chuoke *et al.* [17] found, through comparison with experimental results, the value of $\sigma^*$ to be about eight times the bulk fluid-fluid interfacial tension ($\sigma_{\text{equilibrium}}$) at equilibrium. The approach adopted by Chuoke *et al.* [17] describes cases where the two immiscible fluids involved in the displacement process are separated by a sharp interface, such as is the case in Hele-Shaw cells [18–20]. This approach, however, is merely a first-order approximation for two-phase, immiscible displacements in porous media where capillary forces act over a transition zone rather than a sharp interface. The displacement is not complete and the two phases may flow simultaneously through the pores [18,21]. It is, nonetheless, a first-order approximation, as evident in a number of studies [1,22], to determine whether wavelengths associated with viscous fingers in the experiments are expected to be much greater than the diameter of the core. By using the bulk interfacial tensions reported in Table I and assuming $\sigma^* \approx 8\sigma_{\text{equilibrium}}$, the most prominent finger width for each experiment is calculated and listed in Table II. Importantly, the finger widths predicted by Eq. (7) are much smaller than the diameter of the core used in experiments, and therefore fingers are predicted to emerge during the dynamic displacement process. Although providing some insight, this analysis is insufficient to describe later-time formation and growth of fingers. Shortly, we turn to other methods.

In a recent study, Tang and Kovscek [5] conducted a series of imbibition displacement experiments, using a Berea

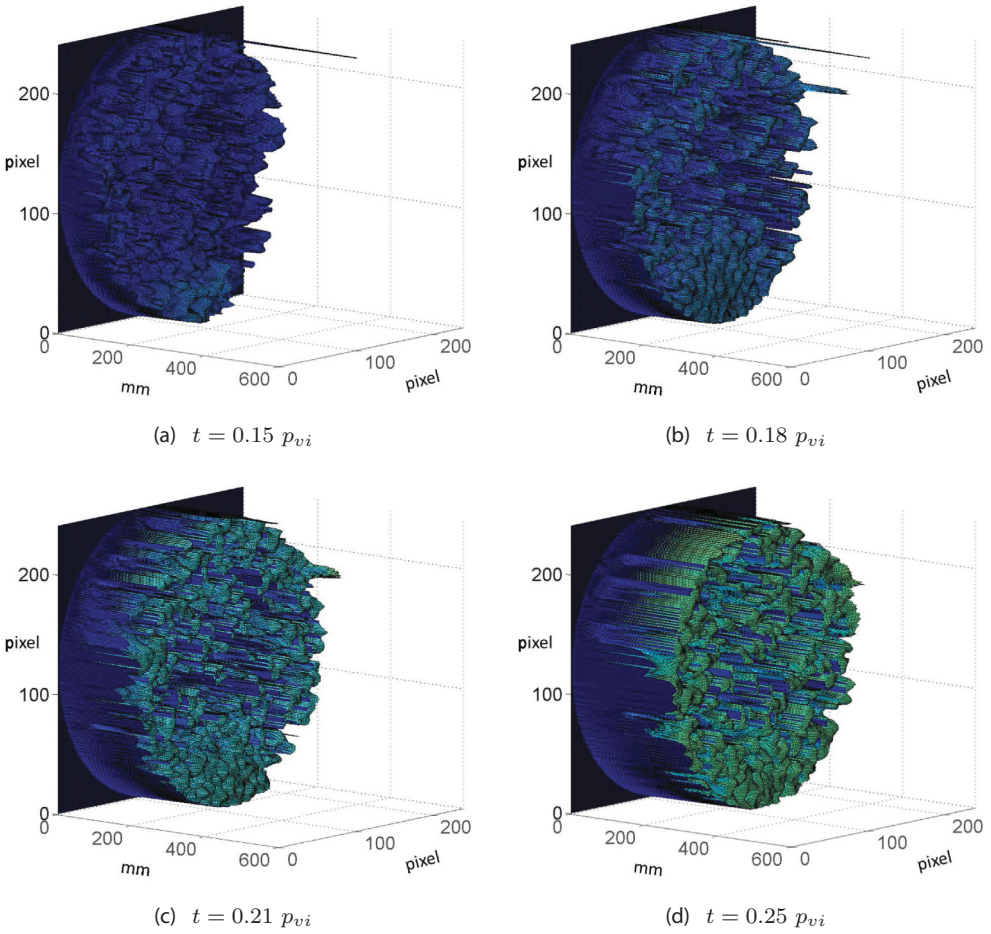


FIG. 5. (Color online) Spatial distribution of shock nonwetting-phase saturation ($S_{nw} = 0.52$) for experiment 5 ($v_r = 4.4$) (a) at time = 0.15 pore volume injected, (b) at time = 0.18 pore volume injected, (c) at time = 0.21 pore volume injected, and (d) at time = 0.25 pore volume injected. In each subfigure, the axis corresponding to the length of the core is represented in millimeters. The other two axes are represented in pixels, where 1 pixel $\approx$ 0.195 mm.

Sandstone core similar in dimension to that used in the present study and a CT scanner to capture the dynamics of flow. The experimental observations were compared with high-accuracy numerical simulations and in-depth and more accurate linear stability analyses [9] similar in formulation to that by Yortsos and Hickernell [18]. It was concluded that the appearance of the reported dominant fingers is supported by the linear stability analysis. In-depth and rigorous analytical and numerical treatments of linear stability analysis have been presented by several authors, i.e., [18,23]. The absence of dominant fingers within the displacement front in this study leads us to take another look at the constitutive relationships for porous media and the continuum equations that describe such phenomena, as discussed next.

### B. Fractal analysis

Fractal dimension ($d_f$) is a measure of the volume of a fractal set with respect to its linear size. The fractal dimension of a solid line or a solid cylinder is a nonfractal set and equals the Euclidean dimension in which it exists. The dimension $d_f$ associated with a set $S$ in a Euclidean space $R^n$ is defined as [24]

$$d_f(S) = \lim_{l \to 0} \frac{\log N(l)}{\log 1/l}, \tag{8}$$

where $N(l)$ represents the number of boxes with side length $l$ required to contain the set fully. If the displacement experiments were perfectly piston-like, sets of $S$ in the experimental results would be right circular cylinders. The volume of such a cylinder is enclosed by the outer surface of the core, with one plane corresponding to the inlet and the other plane corresponding to the surface between the two phases. The displacements, however, are far from perfect cylinders. Sets of $S$ in the experiments reside in $R^3$ Euclidean space and are three-dimensional shapes defined by the outer surface of the core, the inlet plane, and a jagged surface corresponding to the deformations due to instabilities in flow. This uneven surface is defined as a surface comprising points in the medium that have reached prescribed saturation values, selected to represent the shock. The fractal dimensions, as defined in Eq. (8), are calculated for each and every saturation distribution and reported in Table III. Also given are their standard errors of estimation, associated with the regression analysis performed

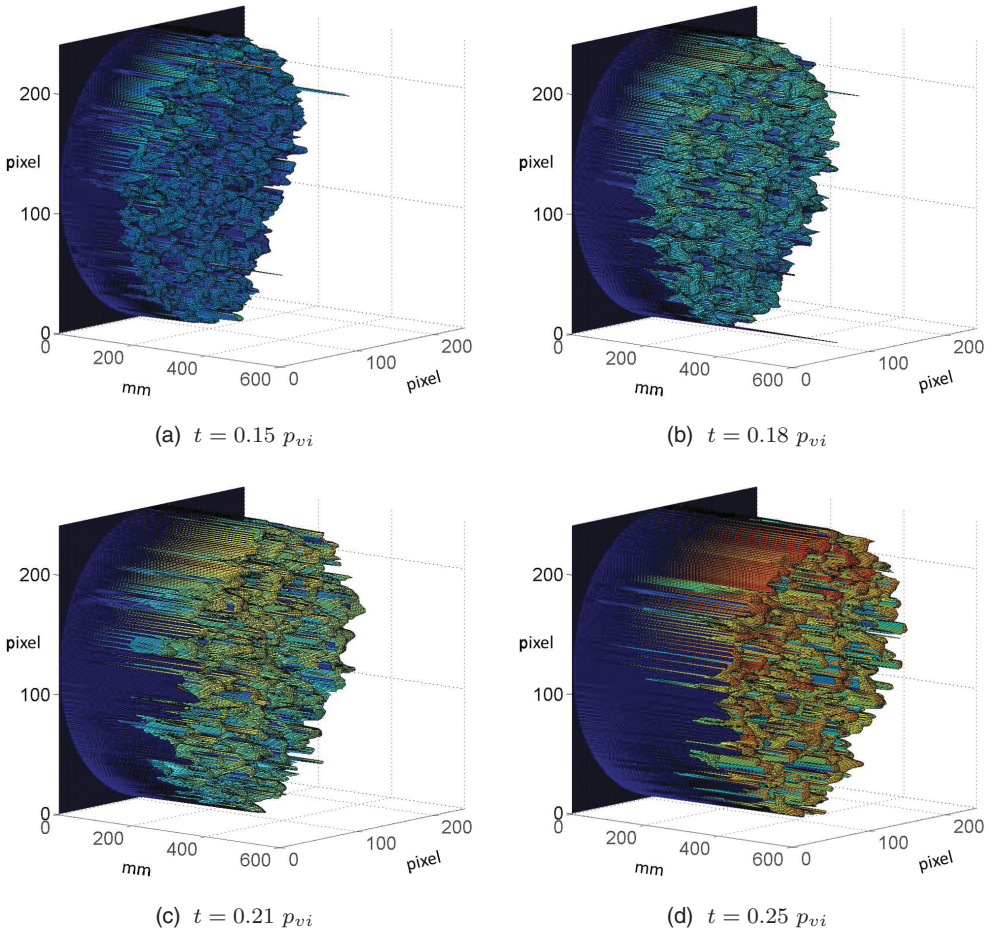


FIG. 6. (Color online) Spatial distribution of shock nonwetting-phase saturation ($S_{nw} = 0.45$) for experiment 6 ($v_r = 15$) (a) at time = 0.15 pore volume injected, (b) at time = 0.18 pore volume injected, (c) at time = 0.21 pore volume injected, and (d) at time = 0.25 pore volume injected. In each subfigure, the axis corresponding to the length of the core is represented in millimeters. The other two axes are represented in pixels where 1 pixel $\approx$ 0.195 mm.

in the calculation of the fractal dimensions [25], defined as

$$s_e = \sqrt{\frac{1}{v}\sum_{i=1}^{n}(\hat{y} - y_i)^2}. \tag{9}$$

Above, $s_e$ is the standard error of estimation, $v$ is the degree of freedom and is equal to the sample size ($n$) minus the number of unknowns estimated by the regression process (in the case of a bivariate regression model such as ours there are two unknowns), $y_i$ is the criterion variable, and $\hat{y}$ is the predicted value of the criterion variable by the regression model.

The evolution of the calculated fractal dimensions as a function of dimensionless time, $p_{vi}$, for all experiments is shown in Fig. 7 using dashed lines. Each subfigure in Fig. 7 highlights the evolution of fractal dimension for one experiment, where dots correspond to points in time when data were collected and the corresponding fractal dimension was calculated and the solid lines connect the dots under the assumption of a linear interpolation between each two adjacent points. At long time, $d_f$ converges to a value of 2.93 to 2.97 depending on the viscosity ratio. For a fractal set embedded in the three-dimensional Euclidean space, the variation of side length $l$ in Eq. (8) is recommended by statisticians to be at least of an order of magnitude of 3 [26,27]; however, unambiguous results may be obtained from the use of data that provide

TABLE II. Width of viscous fingers as predicted by the method of Chuoke *et al.* [17].

| Experiment | $\mu_r$ (cp) | $\mu_i$ (cp) | $\frac{1}{2}\lambda_c$ [a] (mm) | $\frac{1}{2}\lambda_m$ [b] (mm) |
|---|---|---|---|---|
| 1 | 1.05 | 0.92 | 5 | 8 |
| 2 | 1.05 | 0.50 | 2 | 4 |
| 3 | 1.05 | 0.41 | 2 | 3 |
| 4 | 1.05 | 0.33 | 2 | 3 |
| 5 | 1.05 | 0.24 | 1 | 3 |
| 6 | 13.8 | 0.92 | 1 | 1 |
| 7 | 9.2 | 0.92 | 1 | 1 |
| 8 | 18.1 | 0.92 | <1 | 1 |
| 9 | 27.6 | 0.92 | <1 | 1 |
| 10 | 36.0 | 0.24 | <1 | 1 |
| 11 | 13.8 | 32.0 | – | – |

[a]Rounded to nearest integer, calculated using Eq. (6), and assuming $\sigma^* \approx 8\sigma_{\text{equilibrium}}$.

[b]Rounded to nearest integer, calculated using Eq. (7), and assuming $\sigma^* \approx 8\sigma_{\text{equilibrium}}$.

TABLE III. Fractal dimensions ($d_f$) and their corresponding standard errors of estimation ($s_e$) as a function of dimensionless time ($p_{vi}$).

| | | | | | | | | | | | |
|---|---|---|---|---|---|---|---|---|---|---|---|
| | $p_{vi}$ | 0.12 | 0.18 | 0.25 | 0.31 | 0.37 | 0.43 | | | | |
| Expt. 1 | $d_f$ | 2.83 | 2.87 | 2.88 | 2.91 | 2.91 | 2.93 | | | | |
| | $s_e$ | 0.03 | 0.03 | 0.01 | 0.01 | 0.01 | 0.01 | | | | |
| | $p_{vi}$ | 0.09 | 0.12 | 0.18 | 0.21 | 0.25 | 0.28 | 0.31 | 0.34 | 0.37 | 0.40 |
| Expt. 2 | $d_f$ | 2.78 | 2.83 | 2.87 | 2.86 | 2.88 | 2.89 | 2.90 | 2.91 | 2.91 | 2.93 |
| | $s_e$ | 0.05 | 0.04 | 0.02 | 0.02 | 0.02 | 0.02 | 0.01 | 0.01 | 0.01 | 0.01 |
| | $p_{vi}$ | 0.12 | 0.15 | 0.18 | 0.21 | 0.25 | 0.28 | 0.31 | 0.34 | 0.37 | 0.40 |
| Expt. 3 | $d_f$ | 2.85 | 2.83 | 2.86 | 2.90 | 2.91 | 2.92 | 2.92 | 2.93 | 2.93 | 2.94 |
| | $s_e$ | 0.03 | 0.03 | 0.02 | 0.01 | 0.01 | 0.01 | 0.01 | 0.01 | 0.01 | 0.01 |
| | $p_{vi}$ | 0.09 | 0.12 | 0.15 | 0.18 | 0.21 | 0.25 | 0.28 | 0.31 | 0.34 | 0.40 |
| Expt. 4 | $d_f$ | 2.81 | 2.84 | 2.83 | 2.86 | 2.86 | 2.90 | 2.92 | 2.92 | 2.93 | 2.95 |
| | $s_e$ | 0.05 | 0.04 | 0.03 | 0.02 | 0.02 | 0.01 | 0.01 | 0.01 | 0.01 | 0.01 |
| | $p_{vi}$ | 0.09 | 0.12 | 0.15 | 0.18 | 0.21 | 0.25 | 0.28 | 0.31 | 0.34 | 0.37 |
| Expt. 5 | $d_f$ | 2.83 | 2.83 | 2.84 | 2.86 | 2.87 | 2.88 | 2.90 | 2.92 | 2.93 | 2.93 |
| | $s_e$ | 0.05 | 0.04 | 0.03 | 0.03 | 0.02 | 0.02 | 0.01 | 0.01 | 0.01 | 0.01 |
| | $p_{vi}$ | 0.09 | 0.12 | 0.15 | 0.18 | 0.21 | 0.25 | 0.28 | | | |
| Expt. 6 | $d_f$ | 2.68 | 2.77 | 2.83 | 2.89 | 2.90 | 2.90 | 2.92 | | | |
| | $s_e$ | 0.08 | 0.05 | 0.01 | 0.01 | 0.02 | 0.01 | 0.01 | | | |
| | $p_{vi}$ | 0.09 | 0.12 | 0.15 | 0.18 | 0.21 | 0.25 | 0.28 | | | |
| Expt. 7 | $d_f$ | 2.80 | 2.82 | 2.86 | 2.87 | 2.90 | 2.91 | 2.94 | | | |
| | $s_e$ | 0.05 | 0.04 | 0.02 | 0.01 | 0.01 | 0.01 | 0.01 | | | |
| | $p_{vi}$ | 0.06 | 0.09 | 0.12 | 0.15 | 0.18 | 0.21 | 0.25 | 0.28 | | |
| Expt. 8 | $d_f$ | 2.62 | 2.71 | 2.78 | 2.92 | 2.93 | 2.94 | 2.95 | 2.95 | | |
| | $s_e$ | 0.09 | 0.06 | 0.02 | 0.01 | 0.01 | 0.01 | 0.01 | 0.01 | | |
| | $p_{vi}$ | 0.09 | 0.12 | 0.15 | 0.18 | 0.21 | 0.25 | 0.28 | 0.31 | | |
| Expt. 9 | $d_f$ | 2.81 | 2.87 | 2.91 | 2.94 | 2.96 | 2.96 | 2.97 | 2.97 | | |
| | $s_e$ | 0.04 | 0.02 | 0.02 | 0.02 | 0.01 | 0.01 | 0.01 | 0.01 | | |
| | $p_{vi}$ | 0.09 | 0.12 | 0.15 | 0.18 | 0.21 | 0.25 | | | | |
| Expt. 10 | $d_f$ | 2.80 | 2.91 | 2.95 | 2.96 | 2.97 | 2.97 | | | | |
| | $s_e$ | 0.06 | 0.02 | 0.01 | 0.01 | 0.01 | 0.01 | | | | |
| | $p_{vi}$ | 0.09 | 0.12 | 0.15 | 0.18 | 0.21 | 0.25 | 0.28 | 0.31 | | |
| Expt. 11 | $d_f$ | 2.79 | 2.88 | 2.89 | 2.90 | 2.91 | 2.91 | 2.92 | 2.94 | | |
| | $se$ | 0.06 | 0.02 | 0.02 | 0.01 | 0.01 | 0.01 | 0.01 | 0.01 | | |

smaller variations in $l$ [8]. In our case, the maximum possible variation in side length $l$ available in the CT data is restricted to a factor of about 280 by the spatial resolution of the CT scanner. This two-order-of-magnitude variation appears to be sufficient, as demonstrated in Fig. 7.

### C. Scaling of saturation profiles

Invasion percolation as proposed by Wilkinson and Willemsen [28] is a model based on the advancement of a displacement front following the path of least resistance governed by microscale capillary forces under constant flow rate conditions. It was postulated that for an immiscible drainage process, the growth of the volume of the invading nonwetting fluid in a given sphere is proportional to the radius of the sphere raised to the power of the fractal dimension of ordinary percolation, deemed to be approximately 2.5 [8,29]. As a result of the proposed fractal behavior, the nonwetting fluid saturation scales as [8,28,30]

$$S_{nw} \sim L^{d_f-3}, \tag{10}$$

where $L$ is the cluster size. Wilkinson [8] suggests that, if the predicted behavior is not seen in physical observations, a potential culprit is the pressure gradient due to viscous forces. The problem of invasion percolation in the presence of viscous forces has been studied by Xu *et al.* [31] for drainage processes. The case of displacement under large viscosity ratios is described by an extension of the invasion percolation theory, called invasion percolation in a gradient (IPG) [31]. The theory suggests that the width of the viscous invasion front ($w$) is proportional to its propagation velocity. Lam reports results of simple network models to be consistent with percolation theory [32] and validates the assertion of Eq. (10).

We scale saturation profiles observed in drainage displacement experiments following Eq. (10) and assuming $d_f \approx 2.5$ as reported in the literature to be the value of the fractal dimension of invasion percolation-like structures in three dimensions [29,33]. The spatial coordinate $x$ is scaled as

$$Z = (x - \overline{x})/w, \tag{11}$$

where $\overline{x}$ is the middle position of the front and $w$ the width of the front. This scaling, essentially, collapses the spatial

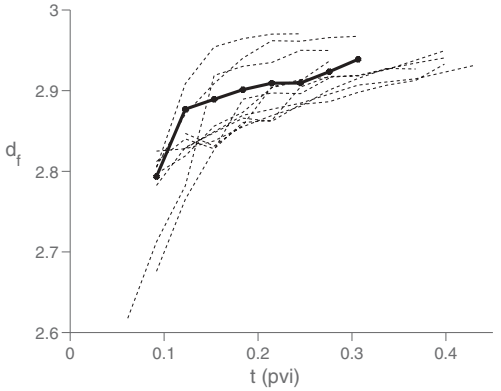


(a) Exp no. 11, $v_r = 0.43$

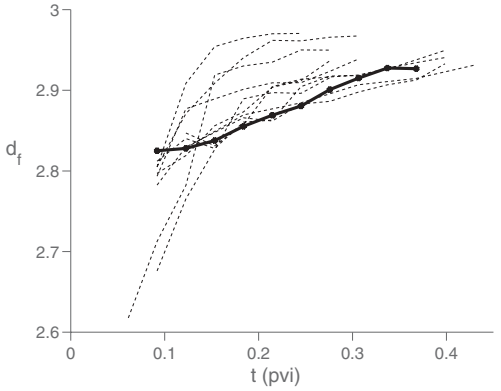


(b) Exp no. 5, $v_r = 4.4$

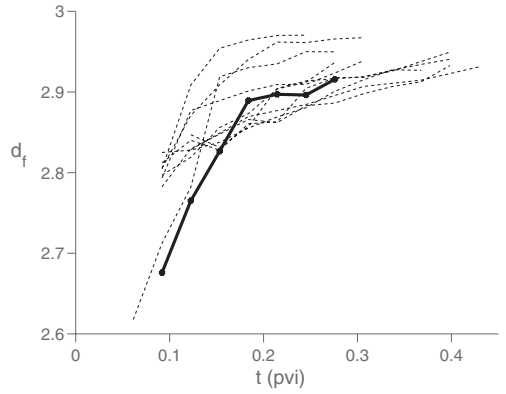


(c) Exp no. 6, $v_r = 15$

FIG. 7. Evolution of fractal dimension with time (pore volumes injected) for all experiments using dashed lines with each subfigure highlighting one experiment: (a) experiment 11 ($v_r = 0.43$), (b) experiment 5 ($v_r = 4.4$), and (c) experiment 6 ($v_r = 15$). Dots correspond to points in time when dynamic saturation data were collected and fractal dimensions calculated. The solid lines connecting the dots outline the time evolution of fractal dimensions under the assumption of linear interpolation between each two adjacent points.

distribution of the leading edge of the fronts of all saturation profiles to one point on the position axis. As evident in Fig. 8, saturation profiles that are scaled as suggested in Eq. (10) do not collapse. In fact, the tightness of the grouping of the scaled profiles appears to have not benefited from the transformation. Such lack of collapse using Eq. (10) is found

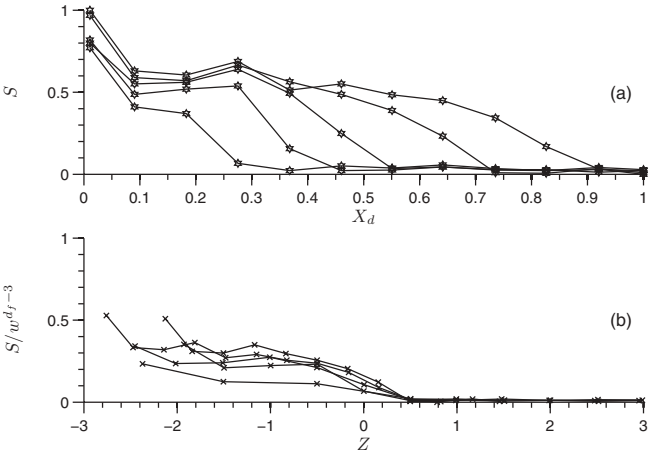


FIG. 8. Experiment 6; viscosity ratio = 15. (a) Evolution of normalized saturation profiles vs position with time; (b) saturation profiles scaled using Eqs. (10) and (11). Roman numerals in subfigure (a) represent times associated with each profile in pore volumes injected: (i) 0.12, (ii) 0.15, (iii) 0.18, (iv) 0.21, and (v) 0.25.

for all experiments described here. It appears that our data are not described by Eqs. (10) and (11).

Additionally, the widths of experimental fronts are plotted on a log-log scale against their corresponding capillary numbers in Fig. 9. The solid line is a linear regression fitted to the data and has a slope of $-9 \times 10^{-4}$. That is, the slope is essentially zero. The experimental front widths and capillary numbers appear to be uncorrelated and our experiments seem to be outside of the flow regime described by IPG.

Alternatively, we seek self-similarity in the experimental saturation profiles inspired by work done by Ferer *et al.* [34] and Sharma *et al.* [35]. The use of fractal dimension in the following scaling relationships for saturation profiles stems from a proportionality between mass of injected fluid and time of injection given a constant injection rate [34], Eq. (12).

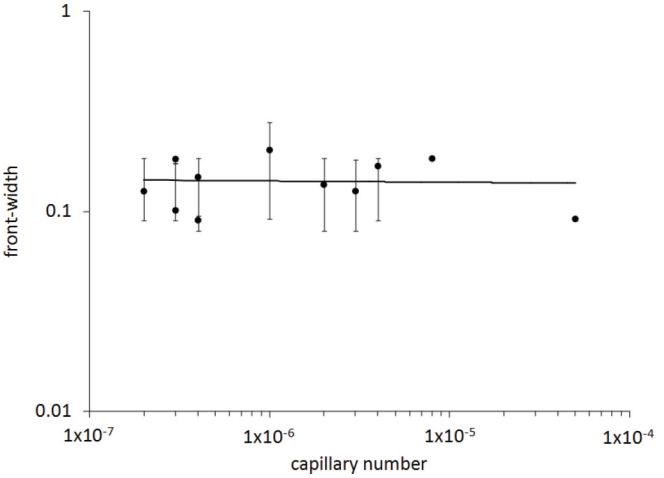


FIG. 9. Plot of experimental front widths vs their corresponding capillary numbers. The front widths are dimensionless using the length of the core as the characteristic length. The error bars represent the range of variation of front widths in each experiment. The solid line is a linear regression fitted to the data (average front widths for each experiment and the corresponding capillary numbers).

This result was revealed through numerical simulations of diffusion-limited aggregation (DLA) [36]. Such models were developed to capture the ramified fractal [37] structures that form and propagate in the spatial domain with time under conditions that promote extreme instabilities, i.e., large ratios of the viscosity of the resident fluid to that of the invading fluid. Such structures have been observed in a large number of experiments using Hele-Shaw cells and artificial porous media, i.e., two-dimensional and quasi-two-dimensional media using glass beads [2,7,15,16,38]. Structures are analyzed using

$$\langle m \rangle \propto t^{1+\epsilon}, \tag{12}$$

where $\langle m \rangle$ is the first moment of mass of the invading fluid, $t$ is injection time under a constant injection rate, and $\epsilon$ is defined as

$$\epsilon = \frac{1}{d_f - 2} - 1. \tag{13}$$

Using this relationship while seeking a self-similar solution to the one-dimensional saturation profiles as they evolve in time, we assume the following homogeneous functional form for saturation [34,35]:

$$S(x,t) = t^u s(x/t^v) \tag{14}$$

and find $u = -\epsilon$ and $v = 1 + \epsilon$; thus, the saturation function scales as

$$S(x,t) = t^{-\epsilon} s(x/t^{1+\epsilon}). \tag{15}$$

Similarly, as demonstrated by Sharma *et al.* [35] and mentioned by Ferer *et al.* [34], the fractional flow function must scale as

$$F(S,t) = f(t^{\epsilon} S). \tag{16}$$

A direct consequence of these scaling relationships is that the constitutive relationships for porous media are functions of both local saturation and time. In other words, the constitutive relationships, namely, relative permeability and capillary pressure functions, are history dependent. Assuming a fractional flow that is solely a function of saturation (classical theory, i.e., extension of Darcy's law to multiphase flow [39]) yields

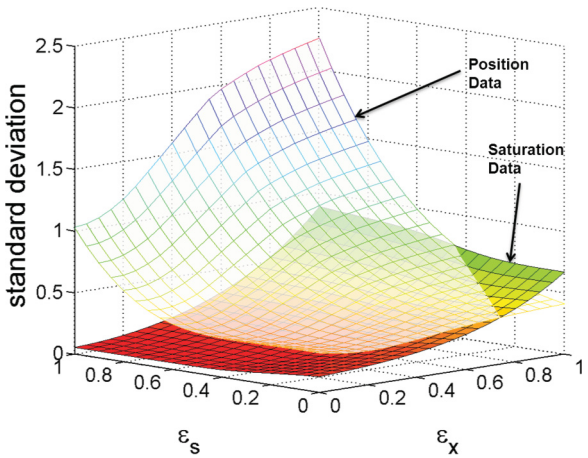


FIG. 10. (Color online) Standard deviation variation due to variation in $\epsilon_x$ and $\epsilon_s$.

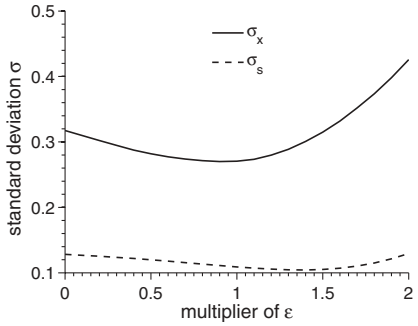


FIG. 11. Standard deviation variation due to variation in $\epsilon$.

the wave speed $(x/t)$ for the saturation profiles,

$$S(x,t) = s(x/t). \tag{17}$$

We investigate self-similarity in the one-dimensional saturation profiles obtained from our dynamic displacement experiments using the following: the wave speed, $x/t$, predicted by classical formulation [Figs. 12(b), 13(b), and 14(b)], and the scaling suggested by Eq. (15), where the saturation values are scaled by $t^{-\epsilon_s}$ and their corresponding one-dimensional position information is scaled by $1/t^{1+\epsilon_x}$.

The two scaling variables, $\epsilon_s$ and $\epsilon_x$, are varied independently and the resulting standard deviation in the saturation

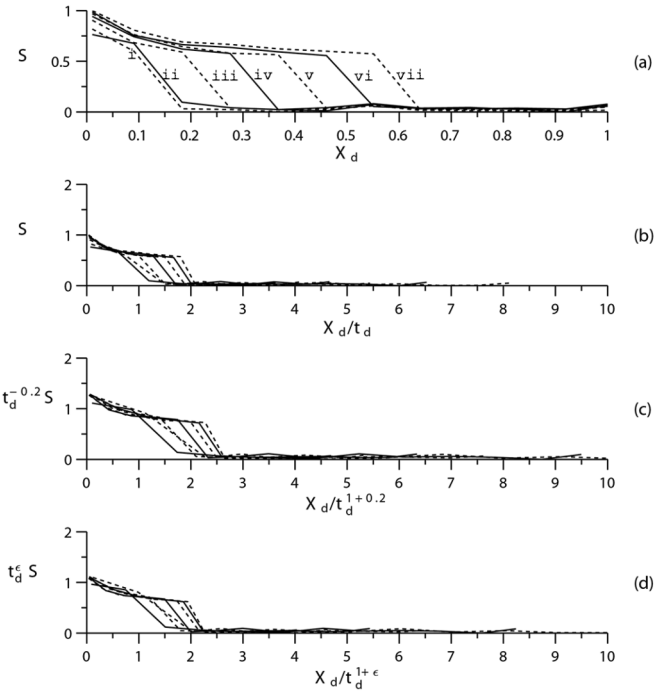


FIG. 12. Experiment 11; viscosity ratio = 0.43. (a) Evolution of normalized saturation profiles vs position with time, (b) saturation profiles scaled using the wave speed, (c) saturation profiles scaled using $\epsilon = 0.2$, and (d) saturation profiles scaled using the fractal dimensions calculated from the experimental three-dimensional saturation distributions (with each profile being scaled using $d_f$ derived from its corresponding three-dimensional saturation distribution). Roman numerals in subfigure (a) represent times associated with each profile in pore volumes injected: (i) 0.12, (ii) 0.15, (iii) 0.18, (iv) 0.21, (v) 0.25, (vi) 0.28, and (vii) 0.31.

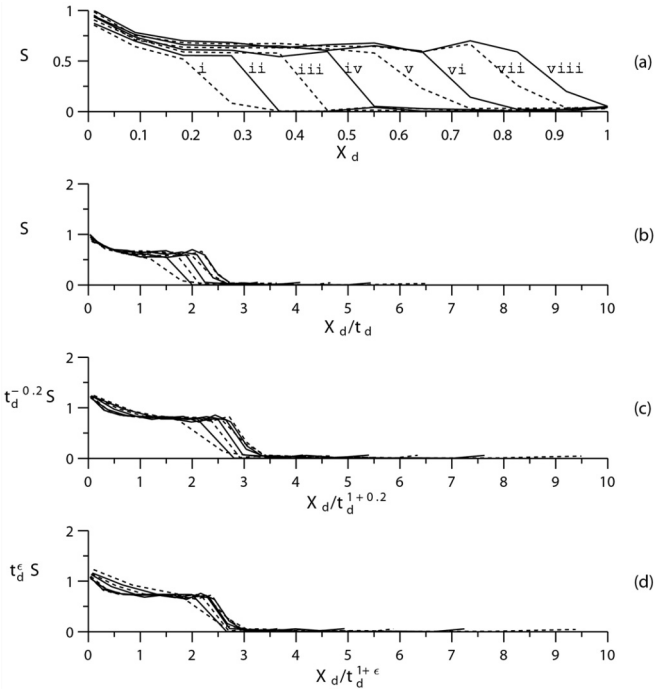


FIG. 13. Experiment 5; viscosity ratio = 4.4. (a) Evolution of normalized saturation profiles vs position with time, (b) saturation profiles scaled using the wave speed, (c) saturation profiles scaled using $\epsilon = 0.2$, and (d) saturation profiles scaled using the fractal dimensions calculated from the experimental three-dimensional saturation distributions (with each profile being scaled using $d_f$ derived from its corresponding three-dimensional saturation distribution). Roman numerals in subfigure (a) represent times associated with each profile in pore volumes injected: (i) 0.15, (ii) 0.18, (iii) 0.21, (iv) 0.25, (v) 0.28, (vi) 0.31, (vii) 0.34, and (viii) 0.37.

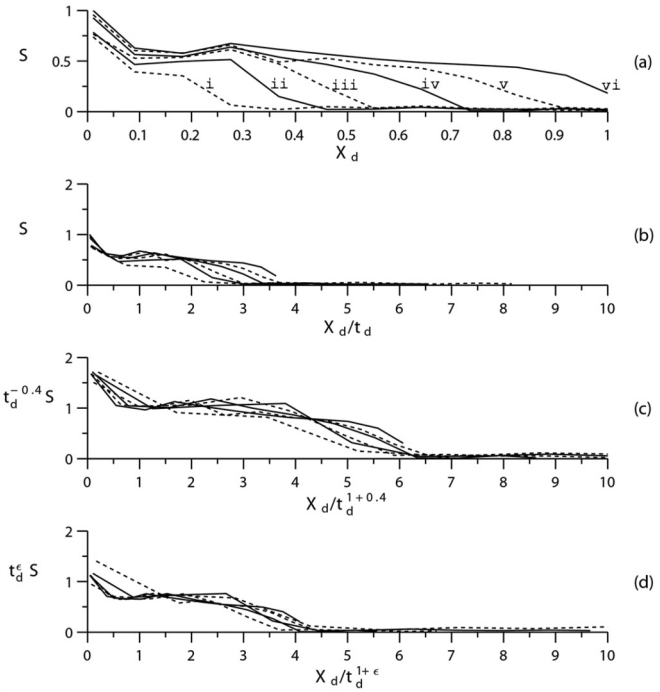


FIG. 14. Experiment 6; viscosity ratio = 15. (a) Evolution of normalized saturation profiles vs position with time, (b) saturation profiles scaled using the wave speed, (c) saturation profiles scaled using $\epsilon = 0.2$, and (d) saturation profiles scaled using the fractal dimensions calculated from the experimental three-dimensional saturation distributions (with each profile being scaled using $d_f$ derived from its corresponding three-dimensional saturation distribution). Roman numerals in subfigure (a) represent times associated with each profile in pore volumes injected: (i) 0.12, (ii) 0.15, (iii) 0.18, (iv) 0.21, (v) 0.25, and (vi) 0.28.

data and their corresponding position data are calculated (see Fig. 10). The intersection of the surfaces represents values of the two scaling variables at which the scaled saturation data and their corresponding position data assume the same standard deviation. For every value of $\epsilon_x$, the smaller the value of $\epsilon_s$ the smaller is the resulting standard deviation in the saturation data. The saturation profiles from each experiment are scaled twice and each time by using the same value for $\epsilon_s$ and $\epsilon_x$:

(1) Based on a sensitivity analysis allowing $\epsilon_s$ and $\epsilon_x$ to vary independently, a singular value is chosen to represent both $\epsilon_s$ and $\epsilon_x$ for all times of each experiment such that the standard deviation of the resulting scaled saturation profiles are minimized [Figs 12(c), 13(c), and 14(c)]. The sensitivity of standard deviations of the saturation and position data using

TABLE IV. Tightness of scaled saturation profiles. Smaller tightness indicates a better fit to the experimental data.

| | Classical | | Fixed exponent | | Variable exponent | |
|---|---|---|---|---|---|---|
| Experiment | Entire profile | Across shock | Entire profile | Across shock | Entire profile | Across shock |
| 1 | 0.220 | 0.324 | 0.205 | 0.317 | 0.194 | 0.245 |
| 2 | 0.171 | 0.257 | 0.162 | 0.186 | 0.141 | 0.161 |
| 3 | 0.276 | 0.406 | 0.251 | 0.385 | 0.200 | 0.200 |
| 4 | 0.250 | 0.387 | 0.215 | 0.352 | 0.193 | 0.180 |
| 5 | 0.250 | 0.360 | 0.236 | 0.358 | 0.202 | 0.224 |
| 6 | 0.282 | 0.330 | 0.319 | 0.384 | 0.266 | 0.276 |
| 7 | 0.214 | 0.288 | 0.172 | 0.248 | 0.151 | 0.111 |
| 8 | 0.170 | 0.258 | 0.159 | 0.206 | 0.135 | 0.189 |
| 9 | 0.322 | 0.460 | 0.300 | 0.450 | 0.208 | 0.270 |
| 10 | 0.310 | 0.378 | 0.278 | 0.344 | 0.200 | 0.261 |
| 11 | 0.204 | 0.365 | 0.226 | 0.401 | 0.197 | 0.339 |

a singular $\epsilon$ for each experiment is also studied by varying the value of $\epsilon$ and capturing the resulting standard deviation, shown in Fig. 11.

(2) The values of $\epsilon$ extracted from saturation distribution maps at each time of each experiment (see Table III) are used in the scaling of each corresponding profile (again by assuming $\epsilon_s = \epsilon_x$) [Figs. 12(d), 13(d), and 14(d)].

As a measure of the degree to which the scaling of the saturation profiles is improved via the inclusion of $\epsilon$ in the scaling factors, the average width of the distribution of the scaled saturation profiles about their mean is calculated for each experiment, once for the entire profile and a second time for the compaction wave (the shock). In Table IV, these average widths, referred to as tightnesses, are reported in the following three categories: (1) classical: classical scaling using wave speed, (2) fixed exponent: scaling using $\epsilon$ values based on the aforementioned sensitivity analysis, and (3) variable exponent: scaling using $\epsilon$ values obtained from experiments. In the last case, each and every profile is scaled using its corresponding fractal dimension.

With the exception of experiments 6 and 11, the use of fixed exponents obtained from sensitivity analyses such as that shown in Fig. 10 improves the tightness of the grouping of the scaled saturation profiles. The use of variable exponents derived from experiments results in tighter grouping of the profiles for all experiments compared to both classical scaling using wave speed and scaling using a single value of $\epsilon$ for all profiles in each experiment. Clearly, scaling relationships using $\epsilon$ are an improvement upon the use of the classical wave-speed scaling relationship. This improvement is more pronounced for displacement fronts with greater viscosity ratios (see Figs. 12 to 14).

## IV. DISCUSSION

Most multiphase flow experiments reported in the literature are performed in artificial two-dimensional or quasi-two-dimensional media, i.e., [2,7]. These processes do not constitute true three-dimensional flows and are not directly comparable to the experiments presented here. In a recent study, Tang and Kovscek [5] conducted a series of imbibition displacement experiments using a Berea Sandstone core and a CT scanner to capture the dynamics of flow. They reported the formation of large-scale viscous fingers and attributed the dispersed nature of the one-dimensional saturation profiles for larger viscosity ratios to macroscopic viscous instabilities. These experimental observations were compared with high-accuracy numerical simulations and linear stability analyses [9] similar in formulation to work done by Yortsos and Hickernell [18]. It was concluded that the appearance of the reported dominant fingers is supported by the linear stability analysis but that the continuum model is deficient in the case of fully developed, unstable forced imbibition. The dimensions of the core used in these experiments are very similar to those used here.

The present study visualizes and analyzes flow instabilities by performing core-scale primary drainage displacement experiments using pairs of immiscible fluids ranging in viscosity ratio from 0.43 to 150 in a homogeneous sandstone. A CT scanner was used to obtain high-resolution, *in situ* images of the flow dynamics and the evolution of saturation profiles in each experiment. One-dimensional saturation profiles show a reduction in the saturation differential associated with the displacement front and an increase in the dispersion of the front as a direct function of the viscosity ratio between the two fluids. Similarly, the chaotic nature of the perturbations of the front and the amount of bypassed resident fluid appear to have a direct relationship with the viscosity ratio.

The results reported in Figs. 3 to 6 lead to the remarkable observation that across a wide range of viscosity ratios the displacement front is relatively smooth and dispersed. For example, even large viscosity ratio displacements at the finest scale of observation (Fig. 6) show a large number of small viscous fingers that reside in the transition zone about the displacement front, and no prominent fingers emerge to engulf the smaller ones. The peak-to-peak separation between these fingers becomes smaller with increasing viscosity ratios and the transition zone becomes more extensive. The striking disagreement between the predictions of linear stability analysis and our observations inspires a renewed approach to formulating the underlying constitutive relationships for porous media [40].

In the classical formulation of multiphase flow in porous media, the complexity of the constitutive relationships is largely ignored and the relationships are assumed to be sole functions of local saturations. One important dimension in the domain of dependence of these relationships (relative permeability and capillary pressure functions) is time. This study finds evidence for time dependence of the constitutive relationships for porous media. As shown in Figs. 12 to 14, experimental one-dimensional saturation profiles were scaled three different ways: once using the wave speed according to the classical formulation and twice using scaling relationships that make fractional flow functions time dependent. The difference between the last two is whether the nature of the time dependence is constant or variable. The use of variably-time-dependent scaling relationships improves the scaled saturation profiles somewhat compared to the other methods (see Figs. 12 to 14). The observed improvement is evidence for the need to provide temporal support in the formulation of fractional flow functions. That is, constitutive relationships evolve with time.

## ACKNOWLEDGMENTS

The authors thank Dr. Silin and his co-workers for our lively discussions. The first author thanks Anne T. and Robert M. Bass for their generous support through the Stanford Graduate Fellowship Program.

[1] E. Peters and D. Flock, SPE J. **21**, 249 (1981).
[2] J. Stokes, D. Weitz, J. Gollub, A. Dougherty, M. Robbins, P. Chaikin, and H. Lindsay, Phys. Rev. Lett. **57**, 1718 (1986).
[3] M. Vives, Y. Chang, and K. Mohanty, SPE J. **4**, 260 (1999).
[4] D. Pavone, SPE Reservoir Eng. **7**, 187 (1992).
[5] G. Tang and A. Kovscek, Transp. Porous Media **86**, 647 (2011).

[6] J.-D. Chen, M. M. Dias, S. Patz, and L. M. Schwartz, Phys. Rev. Lett. **61**, 1489 (1988).
[7] Y. Cinar, A. Riaz, and H. Tchelepi, SPE J. **14**, 588 (2009).
[8] D. Wilkinson, Phys. Rev. A **34**, 1380 (1986).
[9] A. Riaz, G. Q. Tang, H. A. Tchelepi, and A. R. Kovscek, Phys. Rev. E **75**, 036305 (2007).
[10] W. R. Foster, J. Pet. Technol. **25**, 205 (1973).
[11] S. Gupta and S. Trushenski, SPE J. **19**, 116 (1979).
[12] P. Saffman and G. Taylor, Proc. R. Soc. London A **245**, 312 (1958).
[13] S. Hill *et al.*, Chem. Eng. Sci. **1**, 247 (1952).
[14] D. J. Lewis, Proc. R. Soc. London A **202**, 81 (1950).
[15] R. Lenormand, E. Touboul, and C. Zarcone, J. Fluid Mech. **189**, 165 (1988).
[16] J. Nittmann, G. Daccord, and H. Stanley, Nature (London) **314**, 141 (1985).
[17] R. L. Chuoke, P. Van Meurs, and C. Van der Poel, Trans. AIME **216**, 188 (1959).
[18] Y. C. Yortsos and F. J. Hickernell, SIAM J. Appl. Math. **49**, 730 (1989).
[19] L. Schwartz, Phys. Fluids **29**, 3086 (1986).
[20] I. White, P. Colombera, and J. Philip, Soil Sci. Soc. Am. J **40**, 824 (1976).
[21] G. Homsy, Annu. Rev. Fluid Mech. **19**, 271 (1987).
[22] L. Paterson, V. Hornof, and G. Neale, SPE J. **24**, 325 (1984).
[23] A. Riaz and H. Tchelepi, Phys. Fluids **16**, 4727 (2004).
[24] T. Vicsek, *Fractal Growth Phenomena* (World Scientific, Singapore, 1992).
[25] B. Ayyub and R. McCuen, *Probability, Statistics, and Reliability for Engineers and Scientists* (CRC, Boca Raton, FL, 2003).
[26] G. Korvin, *Fractal Models in the Earth Sciences* (Elsevier, Amsterdam, 1992).
[27] H. Henderson and R. Wells, Adv. Geophys. **30**, 205 (1988).
[28] D. Wilkinson and J. Willemsen, J. Phys. A **16**, 3365 (1983).
[29] D. Stauffer and A. Aharony, *Introduction to Percolation Theory* (CRC, Boca Raton, FL, 1994).
[30] R. Chandler, K. Lerman, J. Koplik, and J. Willemsen, J. Fluid Mech. **119**, 122 (1982).
[31] B. Xu, Y. C. Yortsos, and D. Salin, Phys. Rev. E **57**, 739 (1998).
[32] C. Lam, Phys. Rev. Lett. **92**, 254503 (2004).
[33] P. Meakin, A. Birovljev, V. Frette, J. Feder, and T. Jøssang, Physica A (Amsterdam) **191**, 227 (1992).
[34] M. Ferer, W. Sams, R. Geisbrecht, and D. Smith, Physica A (Amsterdam) **177**, 273 (1991).
[35] J. Sharma, S. B. Inwood, and A. R. Kovscek, SPE J. **17**, 1142 (2012).
[36] T. A. Witten and L. M. Sander, Phys. Rev. Lett. **47**, 1400 (1981).
[37] B. Mandelbrot, *The Fractal Geometry of Nature* (Freeman, San Francisco, 1983).
[38] K. Måløy, J. Feder, and T. Jøssang, Phys. Rev. Lett. **55**, 2688 (1985).
[39] M. Muskat and M. W. Meres, Physics **7**, 346 (1936).
[40] S. A. Aryana, Ph.D. thesis, Department of Energy Resources Engineering, Stanford University, 2012.